

# A new technique of characterization of the intrapixel response of astronomical detectors

C. Ketchazo<sup>\*a</sup>, T. Viale<sup>b</sup>, O. Boulade<sup>a</sup>, G. Druart<sup>b</sup>, V. Moreau<sup>a</sup>, L. Mugnier<sup>b</sup>, D. Dubreuil<sup>a</sup>, S. Derelle<sup>b</sup>, S. Ronayette<sup>a</sup>, N. Guérineau<sup>b</sup>, M. Berthé<sup>a</sup>

<sup>a</sup>Service d'Astrophysique, CEA Saclay, Orme des Mérisiers, Gif-sur-Yvette, 91191, France.

<sup>b</sup>ONERA, The French Aerospace Lab, F-91761, Palaiseau, France

## ABSTRACT

This paper is devoted to the presentation of a new technique of characterization of the Intra-Pixel Sensitivity Variations (IPSVs) of astronomical detectors. The IPSV is the spatial variation of the sensitivity within a pixel and it was demonstrated that this variation can contribute to the instrument global error. Then IPSV has not to be neglected especially in the case of under-sampled instruments for high quality imaging and accurate photometry. The common approaches to measure the IPSV consist in determining the pixel response function (PRF) by scanning an optical probe through the detector. These approaches require high-aperture optics, high precision mechanical devices and are time consuming. The original approach we will present in this paper consists in projecting high-resolution periodic patterns onto the whole sensor without classic optics but using the self-imaging property (the Talbot effect) of a Continuously Self Imaging Grating (CSIG) illuminated by a plane wave. This paper describes the test bench and its design rules. The methodology of the measurement is also presented. Two measurement procedures are available: global and local. In the global procedure, the mean PRF corresponding to the whole Focal Plane Array (FPA) or a sub-area of the FPA is evaluated. The results obtained applying this procedure on e2v CCD 204 are presented and discussed in detail. In the local procedure, a CSIG is moved in front of each pixel and a pixel PRF is reconstructed by resolving the inverse problem. The local procedure is presented and validated by simulations. (*Color images and figures in online version*)

**Keywords:** Intra-Pixel Sensitivity Variation, Pixel Response Function, Talbot effect, CSIG, Modulation Transfer Function, Bayesian algorithms

## 1. INTRODUCTION

To achieve wide field of view at an affordable cost, many space-based instruments operate in an under-sampled mode. In this condition, the sub-pixel sensitivity variations can have an important effect, which will be accounted for to obtain good imagery and photometry. The impacts of these variations in sub-pixel scale have been observed in the Wide Field Planetary Camera (WFPC) on the Hubble Space Telescope where the total flux in the stellar image can vary by up to 0.03 mag in F555W WFC images depending on how it sampled. For Near Infrared Camera #3 in WFPC, these variations are up to 0.39 mag and limit its use for stellar photometry [1]. Another example of the influence of the IPSV has been reported in the infrared Array Camera (IRAC) on the Spitzer Space Telescope. The IRAC had been used to measure temporal variations ( $<10^{-4}$ ) in point sources (such as transiting extrasolar planets) at 3.6 and 4.5  $\mu\text{m}$ . Variations of as much as 8 % in sensitivity have been observed as the center of a source moves across a pixel with normal spacecraft pointing wobble and drift [2]. These examples show that a detailed understanding of the detector response is required for the next space missions which aim at achieve wide-field imaging and accurate photometry.

It is the case of the next ESA space mission, Euclid, (an overview of its capabilities can be found in the Euclid Red Book [3]). Euclid is designed to carry out both weak lensing and galaxy clustering cosmological measurements, using a payload comprising a visible imager (VIS) and a near-infrared spectrograph-imager (NIR). Both instruments VIS and NIR cover a field of view of 0.5 deg<sup>2</sup> and are undersampled due to the limited number of detectors in each FPA. Then these instruments could be possibly affected by the IPSV. That is why the IPSV must be precisely evaluated and corrected (if necessary) from the Euclid final images.

Beyond the Euclid project, it is also important to notice that ESA now systematically requires the measurement of the intrapixel sensitivity of detectors under development. Therefore, the purpose of this paper is to present an original experimental technique for the characterization of a large range of astronomical detectors operating from VIS to LWIR.

\*Email : christian.ketchazo@cea.fr

In the following paragraphs, after a state of the art of the main techniques developed to address this subject (section 2), our technique is presented. The technique is designed for the characterization of the visible and near-infrared detectors on a sub-pixel grid of 1/10 of a pixel. Section 3 presents the design rules of our test bench. The methodologies of measurement are presented in detail in section 4 and the first experimental results and simulations are discussed.

## 2. DESCRIPTION OF IPSV MEASUREMENT TECHNIQUES AND COMPARISON

For the measurement of the IPSV, it is important to define the pixel response function (PRF) [4] which is the signal detected by a single pixel when it is illuminated by a point source. Thus PRF is a spatial map of the sensitivity across a pixel, as well as information about the crosstalk between pixels neighbor.

### 2.1 State of the art

The IPSV measurement can be realized either from the astronomical cameras in operation or in laboratory by the characterization of the detectors. In operation conditions, the determination of the PRF involves dithering the camera by a fraction of a pixel over a sequence of exposures. It is then possible to observe how the structure of the objects in the image varies with respect to their positions on the pixel grid. The reconstructed PSF which is the convolution of the optical PSF with the pixel response can be evaluated at any desired fractional pixel location to generate a table of photometric corrections as a function of the relative PSF centroid [1] [2]. In laboratory conditions, the process consists into the projection of an optical probe onto the detector and the measurement of the response of the pixels. Kavalajiev [5] scanned a front-illuminated CCD (FI-CCD) with a small light beam (0.4 -0.5  $\mu\text{m}$  in diameter). They showed difference in response between pixels. Piterman [6] scanned a back-illuminated CCD (BI-CCD) using a light beam with 1.7-3.1  $\mu\text{m}$  FWHM and the bands B, V, I and a narrow one at 470  $\mu\text{m}$ . They showed that the IPSVs are smoother and less wavelength dependent compared with that for FI-CCD. They attributed the difference to the interaction of the light with the gate structures in FI devices. Toyozumi [7] demonstrated that the PRF also depends on the angular distribution of the incoming photon ( $f/\#$ ). In the NIR range, Barron [8] and Biesiadzinski [9] developed a spots projection system “the spots-o-matic” to achieve a two –dimensional scan of pixels in a detector by simultaneously projecting the image of 160k small pinholes onto the detector and then scanning them over several pixels.

These different test benches require high quality, precise and stable opto-mechanical devices. The profiles of the projected probes have to be known and controlled precisely in order to be deconvolved from the measurements. And finally, these measurements are time consuming.

### 2.2 ONERA technique

The technique we present in this paper is based on the Fourier transform approach. The principle is to project high-resolution periodic patterns onto the whole sensor using the self-imaging property (known as the Talbot effect) of a continuously Self-Imaging grating (CSIG) illuminated by a plane wave [10]. The main advantage of this method is that no optics is required to project the target.

Self-imaging principle is technique’s keystone. It basically consists in the faculty of a system to create an image without optic components between the object and the image. In our experience, an “image” is defined by a diffraction of the waves arriving onto the object which then interfere in their recovery area. The obtained interference field presents constructive interferences for which the distribution of the field observed behind the object is reproduced. ONERA developed a new kind of diffracting objects, the CSIGs. When illuminated by a plane wave, a CSIG produces a field whose intensity profile (interferogram) is a propagation-and wavelength-invariant biperiodic array of bright spots (figure 1).

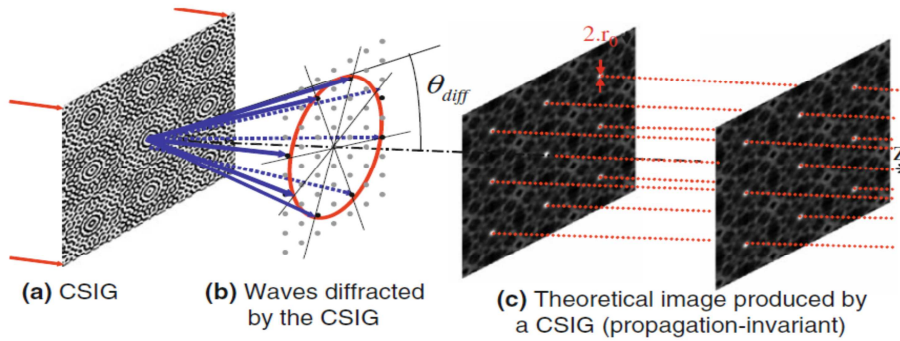


Figure 1 - Illustration of (a) a CSIG, (b) the waves diffracted by the CSIG (blue arrows, whose extremities rely on a circle), and (c) the propagation invariant image produced by the CSIG

The interferogram excites discrete spatial frequencies which allow deducing sub-pixel information via the modulation transfer function. Spatial frequencies excited by the CSIG depends on two factor which will be used for the design of the component: the period  $a_0$  of the CSIG and  $\eta$ , a dimensionless factor which traduce the number of spatial frequencies excited and their coordinates in the Fourier domain.

In the context of the Euclid space mission, the purpose of the technique is to estimate the MTF of our detectors at a spatial frequency equal to 10 times the Nyquist frequency, i.e. 1/10 pixel. The third part of this paper will explain the design rules for CSIG factors ( $a_0$  and  $\eta$ ) to obtain a component allowing reaching the desired accuracy for the Euclid mission.

### 2.3 Experimental protocol and technique's limits

Current technique used in laboratory allows obtaining a MTF for an average pixel corresponding to an area of the detector. The protocol consists in placing in front of the detector to characterize a CSIG illuminated by a parallel beam. Then, by an adapted algorithm (see section 4), which take in account hypothesis on the pixel profile, CSIG parameters ( $a_0$  and  $\eta$ ), and experimental parameters (pinhole diameter, collimator's focal length, spectral emittance), it is possible to deduce an estimation of the real pixel response.

However, the limits of this technique reside in its inability to characterize a pixel-by-pixel response. A solution has been proposed by ONERA which will allow determining the intra-pixel response at the scale of the entire matrix. The principle is to perform a micro-scan following X and Y axis on the matrix in order that each pixel sees a complete pattern of the interferogram. The reconstruction algorithm will be applied to all the pixels simultaneously so an intra-pixel response will be deduce for the entire pixel matrix. The algorithm has been tested by simulations for a square pixel presenting a small defect at its centre.

## 3. DESIGN RULES OF THE TEST BENCH

In this Section, we present the general design rules of the Modulation Transfert Function (MTF) test bench and propose a methodology to characterize the visible (VIS) and near infrared (NIR) detectors on a sub-pixel grid of 1/10 of a pixel.

### 3.1 General description of the Test bench

A light source illuminates a pinhole which is placed in the focal plane of a collimator that produces a parallel beam that impinges the Continuously Self Imaging Grating (CSIG). The grating produces a self-image (or interferogram) in the detection plane. The CSIG is placed at a distance  $d$  from the FPA. See Figure 2.

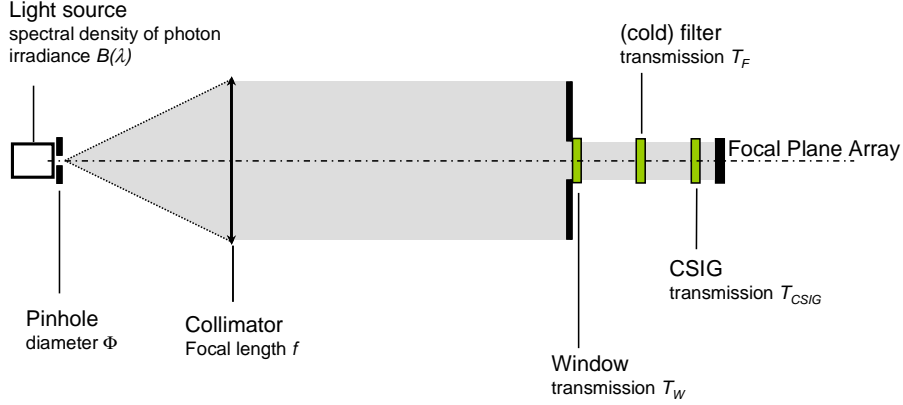


Figure 2 Schematic view of the test bench.

### 3.2 What we have to measure

The final product of measurement is the intra pixel response, that can be seen as a point spread function (PSF) of spatial coordinates  $(x,y)$  :  $\text{PSF}_{\text{pix}}(x,y)$ . The Fourier transform of the PSF yields the pixel's optical transfer function (OTF) of coordinates  $(v_x,v_y)$  (spatial frequencies). The requirement is to determine the PSF on a sub-pixel grid of pitch  $p_{\text{ech}}/M$ , where  $p_{\text{ech}}$  is the sampling pitch of the focal plane array and  $M$  is an over-sampling factor. The extent of the sub-pixel grid is of course spatially limited to a square of typical size  $Kp_{\text{ech}} \times Kp_{\text{ech}}$  (typically  $K=2$  or  $3$ ), size of the pixel PSF support.

Our methodology relies on a sampling of the OTF. If we apply the Nyquist-Shannon sampling theorem, the sampling pitch  $b$  of the OTF has to fulfill the following condition:

$$b = \frac{1}{Kp_{\text{ech}}} \quad (1)$$

On a practical level, the sampling process of OTF is band limited at a cut-off frequency  $v_c$  that corresponds in the space domain to a sampling pitch  $1/(2v_c) = p_{\text{ech}}/M$ . Thus  $v_c$  has to verify the following condition:

$$v_c = \frac{M}{2p_{\text{ech}}} \quad (2)$$

### 3.3 Choosing the CSIG

The CSIG is a two-dimensional diffracting grating. A detailed description of CSIGs and of their properties can be found in [11] and [12]. In this subsection, we only recall fundamental features of CSIGs, which are directly used to design the MTF measurement test bench.

The CSIG excites a set of discrete spatial frequencies in the Fourier domain (Figure 3). All these frequencies are contained in a circle of radius  $v_c$  given by

$$v_c = 2\eta / a_0 \quad (3)$$

$v_c$  corresponds to the maximal spatial frequency which can be measured with a CSIG with parameters  $\eta$  and  $a_0$ . By choosing properly the period of the grating and its orientation with respect to the pixel lines of the detector, aliased spatial frequencies are folded onto frequencies of null amplitude, thus enabling MTF measurement beyond Nyquist frequency of the detector.

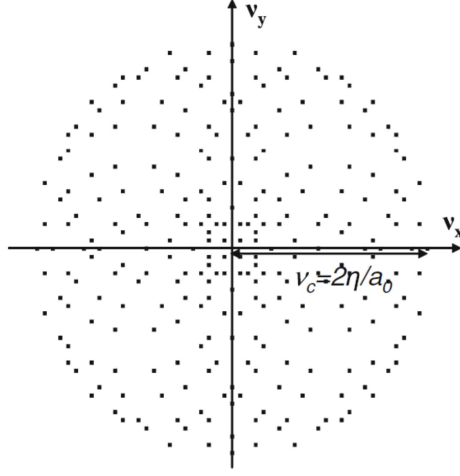


Figure 3: Theoretical OTF of a CSIG. Each spot corresponds to an excited spatial frequency in the Fourier domain

When varying  $\eta$ , the number of orders diffracted by the CSIG changes. For a  $N$ -order CSIG, the number  $N'$  of spatial frequencies of the CSIG's OTF (optical transfer function) is given by [13]:

$$N' = \frac{N^2}{2} + 1 \quad (4)$$

The OTF of the CSIG is composed by sparse delta functions. To compensate for the sparse sampling of the pixel OTF, some regularization is needed in pixel OTF reconstruction. For our application of the pixel OTF measurement, we consider that the searched OTF is continuous and can be recovered from sparsely sampled data with interpolation in the Fourier domain.

As illustrated in Figure 3, the peaks of the CSIG's OTF are sparsely located on a regular grid of pitch  $1/a_0$ . That is why we define a mean pitch  $b_{\text{mean}}$  given by [14]:

$$b_{\text{mean}} = \sqrt{\frac{4\pi\eta^2}{a_0^2} \cdot \frac{1}{N'}} = v_c \sqrt{\frac{\pi}{N'}} \quad (5)$$

As a consequence, if we want to correctly sample the pixel OTF with a ratio  $v/b$  given by Eq. 1 and Eq. 2, the minimum number  $N'$  of peaks of the CSIG's OTF is given by:

$$N'_{\text{min}} = \pi \left( \frac{v_c}{b} \right)^2 \quad (6)$$

Given these previous formulas, we design a CSIG for the characterization of the e2v CCD-204 which is a CCD similar to the Euclid VIS detector [15] with a pixel pitch of  $12 \mu\text{m}$ . To reach the accuracy of the Euclid space mission, we fixed the oversampling factor  $M$  at the value 12 and the extent of the subpixel grid  $K$  at 3. The designed CSIG diffracts 48 orders and corresponds to  $\eta = \sqrt{9425}$ . The CSIG period is equal to  $a_0 = 380 \mu\text{m}$  and the maximal measurable spatial frequency is equal to  $v_c = 511 \text{ mm}^{-1}$ .

### 3.4 Choosing the diameter of the pinhole

The diameter of the pinhole  $\Phi$  has to be chosen with a great care because the pinhole size can impact critically the final image. For example, if the pinhole is too large, it affects the size of the projected pattern because it induces in the final image an additional and undesired filtering effect with a cut-off frequency,  $\rho_{c,\text{pinhole}}$ . In order hands, if the pinhole is too small, the signal-to-ratio would decrease. The pinhole diameter has to be chosen in such a way that  $\rho_{c,\text{pinhole}}$  must be higher than  $v_c$  so that the maximum frequency which can be measured with this setup remains limited by the CSIG, and not by the pinhole.

$$\rho_{c,pinhole} = \frac{1,22}{\Phi'} \quad (7)$$

Where,  $\Phi' = \Phi \cdot d / f$  where  $d$  is the distance between the detector and the CSIG and  $f$  de focal length. We measure directly the distance  $d$  on the test bench as  $d=31.4$  mm and  $f$  is 760 mm. By choosing  $\Phi = 0.05$  mm, then the  $\rho_{c,pinhole} = 591 \text{ mm}^{-1}$ .

### 3.5 Choosing the distance between the CSIG and the detector

The CSIGs are complex objects which cannot be manufactured directly. However a good approximation of these objects can be made with a binary-phase grating. Under polychromatic light of spectral bandwidth  $\Delta\lambda$ , there is a distance at which the achromatic and propagation-invariant regime is reached. This distance  $Z$  is given as:

$$Z = \frac{2a_0^2}{\eta^2 \Delta\lambda} \quad (8)$$

Therefore we have to check on our test bench that the distance  $d$  between the CSIG and the detector is greater than  $Z$ . Our source is a Luxeon white LED with  $\Delta\lambda=0.12 \text{ }\mu\text{m}$  then the panchromatization distance  $Z$  is 0.23 mm which is lower than the distance  $d$ , confirming that we reach on our test bench the achromatic and propagation-invariant regime.

### 3.6 Angular tolerance of a CSIG

In our setup, the CSIG is to be used under normal incidence. However, due to mechanical features, it can be used with a small incident angle, and we have to check that this does not affect the measurement. A study of CSIGs under oblique illumination [16] shows that the maximal incidence angle  $\alpha_c$  of a beam illuminating a CSIG is given by:

$$\alpha_c = \frac{a_0}{\eta} \left( \frac{1}{2\lambda d} \right)^{1/2} \quad (9)$$

Where  $\lambda$  is the illumination wavelength. For incident angles greater than  $\alpha_c$ , the pattern produced by the CSIG suffers from off-axis aberrations (especially astigmatism) which artificially reduce the amplitude of excited spatial frequencies. Under polychromatic illumination, we take the minimal value for the wavelength to determine  $\alpha_c$ . We find  $\alpha_c = 1.3^\circ$ . The angular tolerance imposes the highest constraint in our test bench. But in the present work, we do not address the test bench alignment budget error in accordance with the performances of the mechanical components.

## 4. MEASUREMENT PROCEDURES AND DATA PROCESSING TECHNIQUES

The measurements are based on the projection of a high-resolution periodic pattern into the surface of the FPA using the self-imaging property of a CSIG. Two measurements procedures are available: global and local.

### 4.1 Measurement procedures

In the *global procedure*, the mean PRF corresponding to the whole FPA or a sub-area of the FPA is evaluated. The procedure is based on the assumptions that all the pixels under study are identical. The technique developed to process the data is based on the Fourier domain and consists into the reconstruction of the mean pixel profile by sampling the mean pixel transfer function (PTF). The procedure is explained hereinafter and the experimental results are discussed.

In the *local procedure*, a micro-scanning of the CSIG over at least one of his period is performed so that each pixel could see at least a pattern of the interferogram and it is possible to evaluate the PRF of each pixel by processing the final super-image delivered by each pixel. The micro-scanning is performed following the two axis perpendiculars to the propagation beam axis, and the sampling pitch depends on the accuracy required. The pixel profile is estimated by resolving the imagery inverse problem using a bayesian approach. This procedure is validated by simulations.

In the global procedure, the images presented are acquired with the CCD-204 while in the local procedure, the performances of the CCD-273 (the final Euclid VIS detector) are considered for simulations.

A picture of our evaluation test bench is given at the figure 4. The collimator is an off-axis parabolic mirror, the CSIG is in front of the CCD which is mounted inside the cryostat and cooled to 153 K to reduce the dark current.

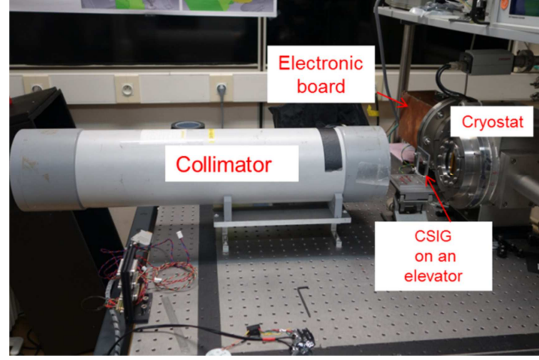


Figure 4: Picture of our test bench

#### 4.2 Reconstruction of the PRF by sampling the PTF – the global procedure

The CSIG is a bi-periodic target. It excites a set of discrete spatial frequencies in the Fourier domain and the input spatial frequency spectrum  $In(\nu)$  can be written as a sum of discrete orders whose components  $D_p^{IN}$  are the Fourier coefficients of the projected periodic pattern:

$$In(\mu, \nu) = \sum_{p, q=-\infty}^{+\infty} D_p^{IN} \delta(\mu - \mu_p, \nu - \nu_q) \quad (10)$$

here  $\delta$  is the Dirac function and,  $\mu_p$  and  $\nu_q$  are the spatial frequencies.

During the image acquisition, the input spatial-frequency spectrum is multiplied by the PTF and replicated at the sampling frequency. By properly choosing the period of the grating and its orientation with respect of the pixel lines of the detector, aliased spatial frequencies are folded onto frequencies of null amplitude, thus enabling PTF measurement beyond the Nyquist frequency. Then during the measurement, the CSIG is canted by an angle  $\theta$ .

The image can be written in the Fourier domain as:  $Out(\mu, \nu) = \sum_{p=-\infty}^{p=+\infty} D_p^{OUT} \delta(\mu - \mu_p, \nu - \nu_p)$ , where  $D_p^{OUT}$  are extracted corresponding to the  $D_p^{IN}$  and the PTF is deduced from:

$$PTF(\mu, \nu) = D_p^{OUT} / D_p^{IN} \quad (11)$$

where the discrete spatial frequencies  $\mu_p$  and  $\nu_q$  are given by:  $p \cdot \sin\theta/a_0$  and  $q \cdot \cos\theta/a_0$ . And therefore, it appears important, for the PTF computation, to determine precisely the values of the parameters  $a_0$ ,  $\theta$  and the position of the center of the CSIG,  $(x_0, y_0)$ .

The image acquired by the CCD is shown in Fig 5. The image is an addition of the bi-periodic projected pattern of the CSIG and the mirrors contributions. In the image, the mirrors contributions are constituted by dusts and stripes. These defects introduce non-homogeneities and blur the image. Nevertheless the long time illumination images present enough contrast to perform the extraction of the Fourier coefficients and to compute the PRF.

The parameters  $a_0$ ,  $\theta$  and the position  $(x_0, y_0)$  of the center of the CSIG pattern with respect to the center of the image are illustrated in Fig 6.

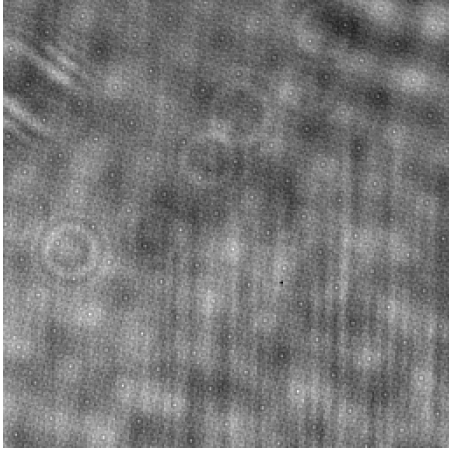


Figure 5. CSIG pattern acquired by the CCD-204. 256x256 pix<sup>2</sup> image

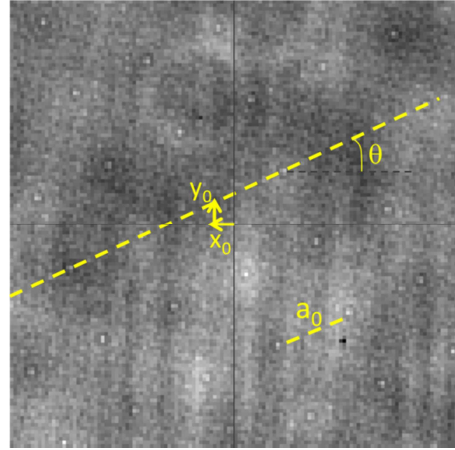


Figure 6 Illustration of  $a_0$ ,  $\theta$  and  $x_0$ , and  $y_0$ . (Zoom in a portion of the image)

The figures 7 and 8 show the mean PRFs reconstructed from the mean pixel transfer function for two-256 x 256 pix<sup>2</sup> sub-areas of the CCD. The PRFs are plotted in a contour representation. The contour levels represent the distribution of the pixel sensitivity. The levels values go from 0. (the most outer) to 0.9 with the 0.5 contour marked in bold. The physical size of the 12 x 12  $\mu\text{m}^2$  pixel is depicted by the red square.

The PRFs present an elongation in the x- and y-directions. The observed asymmetry of the mean pixel sensitivity function is more predominant outside the pixel physical size whereas inside the pixel the sensitivity is symmetric. This behavior can be linked to the CCD effects, basically the diffusion of the charges and the crosstalk between the neighboring pixels. The difference of asymmetry in x- and y-direction can be related to the presence of channel stop. Therefore, the FWHM values differ with the considered direction.

We also notice the difference in morphology between the two PRFs contour plots. This could be due to the presence of dusts in the initial images. These local defects introduce a low-frequency contribution to the data which can be a non-negligible source of errors.

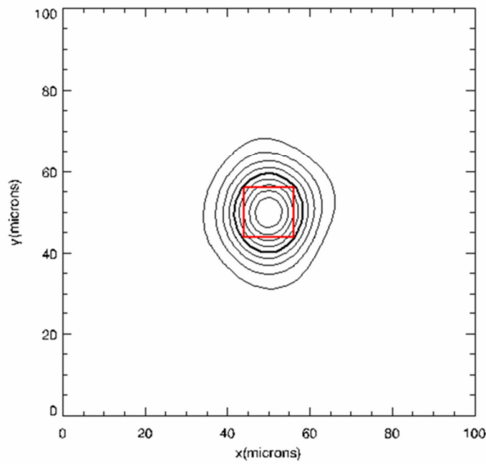


Figure 7: Pixel Response Function reconstructed from the zone 1

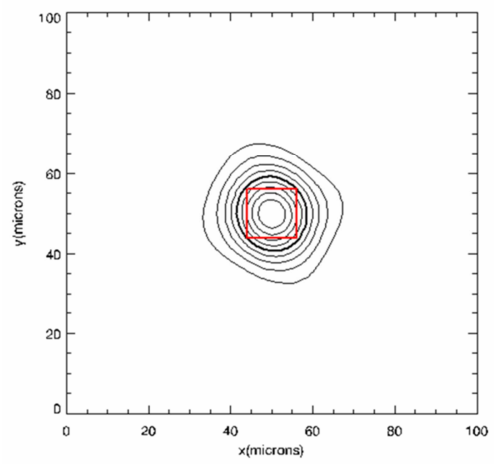


Figure 8: Pixel Response function reconstructed from the zone 2

In the perspectives section (section 5), we present some solutions to improve the quality of the mirrors surface state.

### 4.3 Estimation of the pixel profile – the local procedure

The data processing method developed to evaluate the PRF of the pixel is based on the stochastic approach of the inverse problem. Given an image  $\mathbf{i}$  of an interferogram delivered by a pixel,  $\mathbf{i}$  can be modelled as convolution between  $\mathbf{h}$  the PSF

of the CSIG and  $\mathbf{o}$  the PSF of the detector. The image is also noisy ( $\mathbf{n}$ ). The idea of this method is to operate a deconvolution scheme based on a bayesian approach, which takes into account the noise ( $\mathbf{n}$ ) in the image and the *a priori* information on the object to be restored ( $\mathbf{o}$ ).

This data processing method will be presented in the following paragraph, evaluated and validated by simulations. The validation will consist into a restoration of a pixel profile from a simulated interferogram image. The interferogram image is produced by a direct model.

### The direct model

A summary of the direct model principle is illustrated in the following figure:

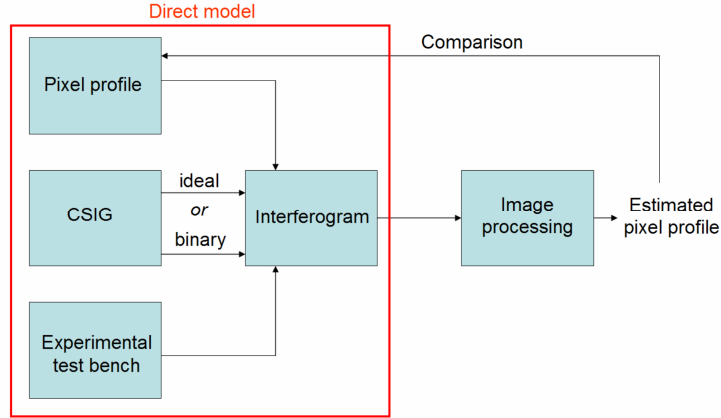


Figure 9: Direct model principle

The direct model produces an interferogram using the following inputs:

- CSIG parameters ( $\eta$ ,  $a_0$ ). The CSIG can be ideal or a binary approximation
- Hypothesis on the pixel profile: In this model, the pixel is a square of size equal to the pixel pitch of the detector and has a defect somewhere in the area of the square and whose amplitude is a ratio of the amplitude of the square pixel. The profile of the defect can be either a small square or a Gaussian profile with a full width at half maximum corresponding to  $p_{ech}/M$ . An illustration of a theoretical pixel profile is given in Figure 4. This profile has a small defect at the centre.
- Experimental parameters: pinhole diameter, collimator's focal length, light spectral emittance, distance between the CSIG and the detector

The produced interferogram will then be treated to get an estimated pixel profile. The result of the image processing giving an estimated pixel profile is then compared to the theoretical pixel profile.

### Interferogram and pixel profile simulations

The Point Spread Function (PSF) of the CSIG, obtained from the binary mask ( $\eta = \sqrt{9425}$  and  $a_0 = 380\mu\text{m}$ ), is calculated. The PSF is a polychromatic one taking into account the spectrum of the source (M625F1Thorlabs Fiber-coupled source). Then, we convolve in the Fourier domain the PSF with the shape of the pixel and with the shape of the image of the source in the focal plane. Finally, we add some noise on the interferogram. The evaluation of the radiometric budget of the test bench has demonstrated that a SNR of 500 in the image is required to perform the calculations. The distance between the CSIG and the detector is 10 mm. The image of the source is a circle of diameter  $\Phi'$  equal to  $1.3\mu\text{m}$ . The pixel pitch of the interferograms is  $1\mu\text{m}$ .

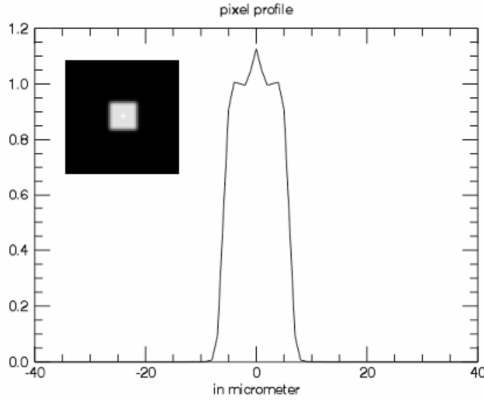


Figure 10: Example of pixel's theoretical profile taken into account in the direct model.

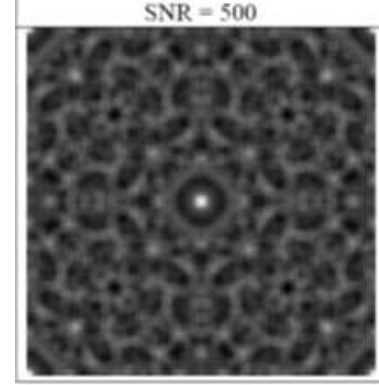


Figure 11: Example of interferograms produced by our direct model for different SNR.

Let  $\mathbf{i}$  the image of the CSIG (or interferogram) recorded by the sensor, this image can be modelled as:

$$\mathbf{i} = (\mathbf{h} * \mathbf{o}) \diamond \mathbf{n} \quad (8)$$

where  $\mathbf{h}$  is the PSF of the CSIG,  $\mathbf{o}$  is the sought PSF of the detector, which is our object of interest for the problem at hand (called *object* in the following), and the symbol  $\diamond$  represents a pixel-by-pixel operation. If the noise is additive and independent of the noiseless image  $\mathbf{h} * \mathbf{o}$ , then the symbol  $\diamond$  simply represents addition. The problem is to obtain an estimate  $\hat{\mathbf{o}}$  of the observed object  $\mathbf{o}$  given the image  $\mathbf{i}$ , a precise knowledge of the CSIG's PSF  $\mathbf{h}$ , as well as some prior information on the noise statistics and on the object (the sought detector PSF).

Following the Bayesian Maximum à Posteriori approach, the deconvolution problem can be stated as follow: we look for the most likely object given the observed image  $\mathbf{i}$  and our prior information on  $\mathbf{o}$ , which is summarized by probability density  $p(\mathbf{o})$ . This reads:

$$\hat{\mathbf{o}} = \arg \max p(\mathbf{o} | \mathbf{i}) = \arg \max p(\mathbf{i} | \mathbf{o}) \times p(\mathbf{o}) \quad (9)$$

Equivalently  $\hat{\mathbf{o}}$  can be defined as the object that minimizes a compound criterion  $J(\mathbf{o})$  defined as:

$$J(\mathbf{o}) = J_i(\mathbf{o}) + J_o(\mathbf{o}) \quad (10)$$

here the negative log-likelihood  $J_i = -\ln p(\mathbf{i} | \mathbf{o})$  is a measure of fidelity to the data

$$J_i^{mix}(\mathbf{o}) = \sum_{l,m} \frac{1}{2\sigma^2(l,m)} [\mathbf{i}(l,m) - (\mathbf{o} * \mathbf{h})(l,m)]^2 \quad (11)$$

where  $\sigma^2(l,m) = \sigma_{ph}^2 + \sigma_{det}^2$  is the sum of the photon noise and the detector noise variances. The variance  $\sigma_{det}^2$  and the variance map  $\sigma_{ph}^2(l,m)$  can both be estimated from the image.  $J_o = -\ln p(\mathbf{o})$  is a regularization or penalty term. We choose a Gaussian prior probability distribution for the object. In this case, a reasonable model of the object's power spectral density (PSD) with only 3 parameters can be found [17] and used to derive the regularization criterion  $J_o$ . The noise is assumed to be approximately stationary with  $\sigma^2$  as a variance. We use a maximum-likelihood approach to estimate this 4 parameters (3 for the object and one for the noise) and then perform the restoration in a fully unsupervised way i.e. without having to tune any parameter manually.

The criterion  $J$  (Eq. (10)) is minimized numerically to obtain the MAP estimate for the object  $\mathbf{o}$ . The minimization is performed by a quasi-Newton method known as VMLM-B for Variable Metric with Limited Memory and Bounds [18].

Some reconstruction results are given in the following figures. The considered interferogram image  $i$  is the one delivered by the direct model. The SNR is equal to 500: the image minimum, average and maximum values are respectively 349, 459 and 780 ADU, and the noise standard deviation is 0.92.

The figure below shows, in false colours (with the standard rainbow look-up table), the  $36 \times 36$  central pixels of the true object, of the noisy interferogram used as input of the restoration, and of two restorations: the unsupervised Wiener restoration, where the PSD has been estimated by maximum likelihood but no constraint is used, and the restoration with unsupervised PSD estimation, positivity constraint and support constraint (36 pixels, i.e.  $36 \mu\text{m}$ ). The latter is quite satisfactory, as shown more quantitatively in the next two figures.

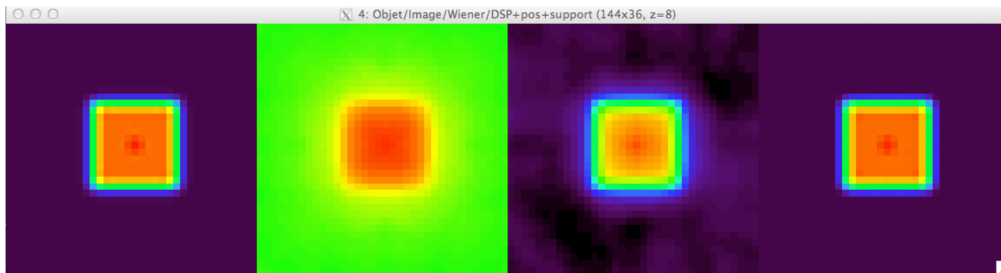


Figure 12: From left to right: images ( $36 \times 36$  pixels, i.e.  $36 \times 36 \mu\text{m}^2$ ) of the true object, the noisy interferogram and two restorations

The figure below shows a horizontal profile of the true object and the various restorations. Clearly, the positivity constraint brings a dramatic improvement with respect to the simple Wiener filter. And adding the support constraint, although the support is (on purpose) quite large, further improves the restoration (see the blue curve vs. the green one).

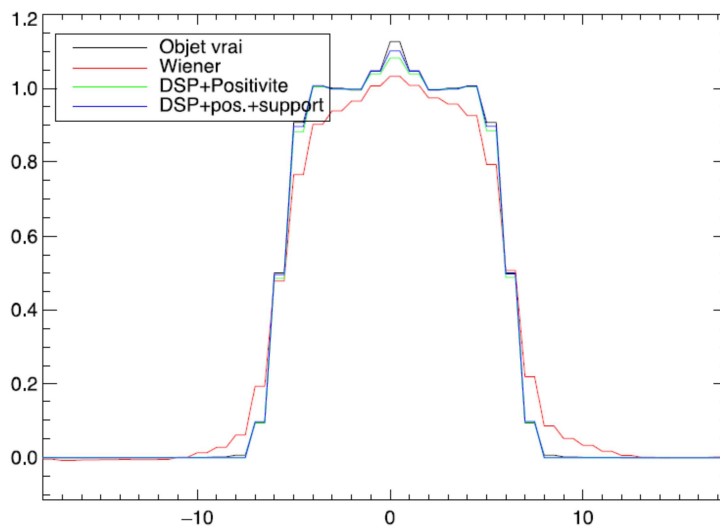


Figure 13: Horizontal profiles of the true object and various estimations.

The following figure shows the true object, the restored one, and 50 times the absolute value of the difference, all with the same dynamic range. The maximum error is thus of the order of 2% (2.4%), and is located at the center of the pixel; the RMS error on the  $36 \times 36$  support is well below 1% (0.3%).

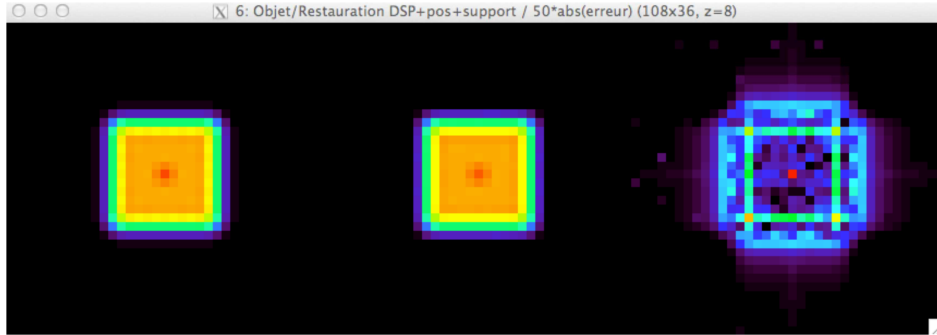


Figure 14: Images of true object, the restored one, and 50 times the absolute value of the difference (from the left to the right). SNR = 500

## 5. PERSPECTIVES

The CEA approach is to use a single test bench to perform the Intrapixel characterization for all the different detectors from the visible to the Mid Infrared range. So the goal of the optical bench is to ensure the stability and the optical quality required for the intrapixel measurements on the large spectral band coverage from  $0.4 \mu\text{m}$  to  $12 \mu\text{m}$ . The use of mirrors, achromatic, is straightforward. The maximum mechanical stability will be achieved by fixing all the components, optics and detector, to the same mechanical structure, inside a cryostat. The cryostat could be a DN630 in Inox 304 with a Sumitomo type cryogenerator constituted by 2 stages delivering  $5.4 \text{ W}$  and  $30 \text{ W}$  respectively at  $10$  and  $45 \text{ K}$ .

The optical design is shown in Figure 12.

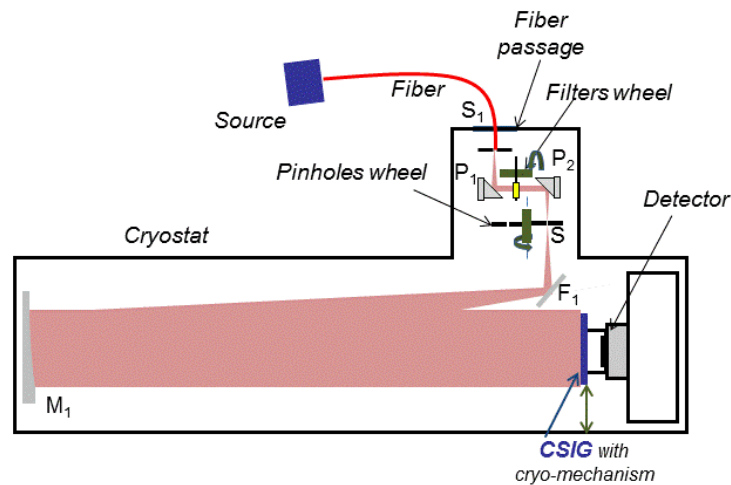


Figure 15. Optical layout of the optical bench planned by CEA for intrapixel characterization of detectors from the visible range to the MID Infrared range.

The pinhole  $S$  is at the focus of the off-axis parabolic  $M_1$  mirror delivering a plane wavefront on the CSIG.  $F_1$  is a folding mirror for compactness purpose. To avoid thermal emission straylight, the source is put outside the cryostat, the light being introduced through a fiber. The couple of off-axis parabolic mirrors,  $P_1$  and  $P_2$ , in aluminium alloy, deliver an achromatic image of the output of the fiber  $S_1$  to the pinhole  $S$ . At this level of the study the design is as flexible as possible and a pinholes wheel and a mid-infrared filters wheel are planned. All components will be fixed to the same mechanical structure.

From our experience in the Mid Infrared instrumentation<sup>i</sup> we know that by manufacturing the mirrors as a single component with their mounting and by using the same material, aluminum alloy 6061 or 5083, as for the optical bench, no setting is necessary when cooling down from the room temperature to the cryogenic temperature. The homogeneity of the shrinking, distance and power of the mirror, keeps the pinhole at the off-axis parabolic mirror focus. To obtain a high

quality surface state, the mirrors have to be treated by laser post polishing technique after a deposition of a nickel coating.

According to the detector under study, the CSIG, the fiber and the source will be changed without changing the optical setup. Table 1 summarizes the sources and the fibers which could be used.

Table 1. List of sources and fibers which will be used according to the spectral band.

<i>Band</i>	<i>Sources</i>	<i>Fibers</i>
0.616 $\mu\text{m}$ – 0.634 $\mu\text{m}$	Visible 1, M625F1	Thorlabs Fiber-coupled source
0.768 $\mu\text{m}$ – 0.793 $\mu\text{m}$	Visible 2, M780F1	Thorlabs Fiber-coupled source
1.02 $\mu\text{m}$ – 1.08 $\mu\text{m}$	NIR 1, M1050F1	NIR-Silica fiber
1.40 $\mu\text{m}$ – 1.50 $\mu\text{m}$	NIR 2, LED 1450E	Chalcogenide Infra-red fiber (CIR)
1.78 $\mu\text{m}$ – 1.93 $\mu\text{m}$	NIR 3, LED 1800P	Chalcogenide Infra-red fiber (CIR)
Mid IR [7 $\mu\text{m}$ -11 $\mu\text{m}$ ]	Heraeus	Polycrystalline Infra-red fiber (PIR)

Thermal analysis will be performed to determinate the cryogenic temperature required to make thermal emission negligible with respect to the detector noise.

## 6. CONCLUSION

We have presented an original technique for the characterization of the intrapixel response of astronomical detectors.

This technique used a diffracting component, the CSIG, and consists in the projection of a bi-periodic pattern onto the detector without classic optics. We have designed and manufactured a high-resolution CSIG to fulfill the requirements of astronomical missions. The component has been integrated into an evaluation test bench and the characterizations have been carried in the visible range onto the e2v CCD-204. Our first measurement procedure consists into the reconstruction of the mean PRF corresponding to a dedicated sub-area of detector. The reconstruction of the PRF takes in account the modulus and the phase of the pixel Transfer function. The first result show that the mean pixel sensitivity function is circular inside the physical size of the pixel and asymmetric outside the pixel. We attribute this behavior to the charge transfer inside the detector and the crosstalk between neighboring pixels.

We have developed a second procedure which consists to perform a X-Y micro-scan at the subpixel scale through the FPA in order that each pixel sees an entire pattern. And then processing each image pixel (one-period interferogram), each pixel sensitivity can be estimated. The approach has been validated by simulations using a method based on the Bayesian approach.

The next step will consist to develop a single test bench to perform IPSV characterization for all types of detectors from VIS to the NIR, by just changing the source and the CSIG. For thermal and mechanical stabilities, the test bench will be integrated inside a cryostat and the optical components will be manufactured in the same material.

We have received the funding from the DIM-ACAV and the LabEx P2IO, for the development of the test bench. This test bench will be available around the mid-2015.

## 7. ACKNOWLEDGEMENTS

This work has been partially supported by the LabEx FOCUS ANR-11-LABX-0013 and the CNES, the French national space agency. The authors thank the European Space Agency which provides the CCD-204.

The development of the final test bench is supported by the DIM-ACAV and the LabEx P2IO.

## 8. BIBLIOGRAPHY

- [1] T. R. Lauer, “The photometry of undersampled point spread functions,” *Publications of the Astronomical Society of the pacific*, vol. 111, no. 765, pp. 1434-1443, 1999.
- [2] J. G. Ingalls, J. E. Krick, S. J. Carey, S. Laine, J. A. Surace, W. J. Glaccum, C. C. Grillmair and P. J. Lowrance, “Intra-pixel gain variations and high-precision photometry with the Infrared Array Camera (IRAC),” *SPIE*, vol. 8442, no. 84421Y, pp. 1-13, 2012.
- [3] R. Laureijs, “Euclid Definition Study Report,” 2011.

- [4] D. Kavaldjiev and Z. Ninkov, "Influence of nonuniform charge-coupled device pixel response on aperture photometry," *Opt. Eng.*, vol. 40, no. 2, pp. 162-169, 2001.
- [5] D. Kavaldjiev and Z. Ninkov, "Subpixel sensitivity map for a charge-coupled device sensor," *Opt. Eng.*, vol. 37, no. 3, pp. 948-954, 1998.
- [6] A. Piterman and Z. Ninkov, "Subpixel sensitivity maps for a back-illuminated charge-coupled device and the effects of nonuniform response on measurement accuracy," *Opt. Eng.*, vol. 41, no. 6, pp. 1192-1202, 2002.
- [7] H. Toyozumi and M. C. Ashley, "Intra-pixel sensitivity variation and charge transfer inefficiency - Results of CCD scans," *the Astronomical Society of Australia*, vol. 22, pp. 257-266, 2005.
- [8] N. Barron, M. Borysow, K. Beyerlein, M. Brown, C. Weaverdyck, W. Lorenzon, M. Schubnell, G. Tarlé and A. Tomasch, "Sub-pixel response measurement of near-infrared sensors," *Publ. Astron. Soc. Pac. (PASP)*, vol. 119, pp. 466-475, 2007.
- [9] T. P. T. G. Biesiadzinski, M. J. S. M. Howe, W. Lorenzon, C. Weaverdyck and J. Larson, "A method for the characterization of subpixel response of near-infrared detectors," *Proc. of SPIE*, vol. 7742, no. 77421M, pp. 1-9, 2010.
- [10] N. Guérineau, S. Rommeluère, E. di Mambro, I. Ribet and J. Primot, "New techniques of characterisation," *C. R. Physique*, vol. 4, pp. 1175-1185, 2003.
- [11] N. Guérineau, B. Harchaoui, J. Primot and K. Heggarty, "Generation of achromatic and propagation-invariant spot arrays by use of continuously self-imaging gratings," *Optics Letters*, vol. 26, no. 7, pp. 411-413, 2001.
- [12] N. Guérineau and J. Primot, "Nondiffracting array generation using an N-wave interferometer," *J. Opt. Soc. Am. A*, vol. 16, no. 2, pp. 293-298, 1999.
- [13] M. Piponnier, G. Druart, N. Guérineau, J.-L. de Bougrenet and J. Primot, "Optimal conditions for using the binary approximation of continuously self-imaging gratings," *Optics Express*, vol. 19, no. 23, 2011.
- [14] R. Horisaki, M. Piponnier, G. Druart, N. Guérineau, J. Primot, F. Goudail, J. Taboury and J. Tanida, "Regularized image reconstruction for continuously self-imaging gratings," *Applied Optics*, vol. 52, no. 16, 2013.
- [15] M. Cropper, R. Cole, A. James, Y. Mellier, J. Martignac, A.-M. di Giorgio, S. Paltani, L. Genolet, J.-J. Fourmond, C. Cara, J. Amiaux, P. Guttridge, D. Walton, P. Thomas, K. Rees, P. Pool, J. Endicott, A. Holland, J. Gow, N. Murray, L. Duvet, J.-L. Augueres, R. Laureijs, P. Gondoin, T. Kitching, R. Massey, H. Hoekstra and Euclid Collaboration, "VIS: the visible imager for Euclid," *Intrumentation and methods for astrophysics*, 2012.
- [16] G. Druart, N. Guérineau, R. Haïdar, J. Primot, P. Chavel and J. Taboury, "Nonparaxial analysis of continuous self-imaging gratings in oblique illumination," *J. Opt. Soc. Am. A*, vol. 24, no. 10, pp. 3379-3387, 2007.
- [17] J.-M. Conan, L. Mugnier, T. Fusco, V. Michau and G. Rousset, "Myopic deconvolution of adaptive optics images by use of object and point-spread function power spectra," *Applied Optics*, vol. 37, no. 21, pp. 4614-4622, 1998.
- [18] E. Thiébaud, "Optimization issues in blind deconvolution algorithms," *Astronomical Data Analysis*, vol. 4847, pp. 174-183, 2002.

---

<sup>i</sup> Ref MIRI et VISIR